mathematics

Article

Finite Element Study for Magnetohydrodynamic (MHD) Tangent Hyperbolic Nanofluid Flow over a Faster/Slower Stretching Wedge with Activation Energy

Bagh Ali [1,†], Rizwan Ali Naqvi [2,†], Amna Mariam [3], Liaqat Ali [4] and Omar M. Aldossary [5,*]

1 Department of Applied Mathematics, Northwestern Polytechnical University, Xi'an 710129, China; baghalisewag@mail.nwpu.edu.cn
2 Department of Intelligent Mechatronics, Sejong University, Seoul 100083, Korea; rizwanali@sejong.ac.kr
3 School of Mathematics, National College of Business Administration and Economics Lahore Layyah Campus, Layyah 31200, Pakistan; amnamariam22sep@gmail.com
4 School of Energy and Power, Xi'an Jiaotong University, No. 28 Xianning West Road, Xi'an 7100049, China; math1234@stu.xjtu.edu.cn
5 Department of Physics and Astronomy, College of Science, King Saud University, P.O. Box 2455, Riyadh 11451, Saudi Arabia
* Correspondence: omar@ksu.edu.sa
† Bagh Ali and Rizwan Ali Naqvi are Co-first author, these authors contributed equally to this work.

Abstract: The below work comprises the unsteady flow and enhanced thermal transportation for Carreau nanofluids across a stretching wedge. In addition, heat source, magnetic field, thermal radiation, activation energy, and convective boundary conditions are considered. Suitable similarity functions use to transmuted partial differential formulation into the ordinary differential form, which is solved numerically by the finite element method and coded in Matlab script. Parametric computations are made for faster stretch and slowly stretch to the surface of the wedge. The progressing value of parameter A (unsteadiness), material law index ϵ, and wedge angle reduce the flow velocity. The temperature in the boundary layer region rises directly with exceeding values of thermophoresis parameter Nt, Hartman number, Brownian motion parameter Nb, ϵ, Biot number Bi and radiation parameter Rd. The volume fraction of nanoparticles rises with activation energy parameter EE, but it receded against chemical reaction parameter Ω, and Lewis number Le. The reliability and validity of the current numerical solution are ascertained by establishing convergence criteria and agreement with existing specific solutions.

Keywords: finite element method; tangent hyperbolic nanofluid; falkner-skan flow; wedge geometry; activation energy

check for updates

Citation: Ali, B.; Naqvi, R.A.; Mariam, A.; Ali, L.; Aldossary, O.M. Finite Element Study for Magnetohydrody namic (MHD) Tangent Hyperbolic Nanofluid Flow over a Faster/Slower Stretching Wedge with Activation Energy. *Mathematics* **2021**, *9*, 25. https://dx.doi.org/10.3390/math9010025

Received: 4 November 2020
Accepted: 12 December 2020
Published: 24 December 2020

1. Introduction

In the past few decades, the discovery of nanoparticles has to define another goal for researchers. A new roadmap has been launch to create a useful energy source. The foundation of modern technologies has been laid. The interesting noteworthy of these nanoparticles is identified with the advancements of solar energy systems, semiconductors, biomedical engineering, energy, pharmaceutical products, and materials manufacturing, etc. Generally, nanofluids are other types of fluid mixed with nanoparticles through conventional doping fluids (oil, water, gels, and polymers). These nanoparticles are mostly composed of metals, oxides, starches, nitrides, and non-metals, measuring somewhere between 1 and 100 nm. The fluid utilized in modern high technological areas with huge heat diffusivity capacity is called nanofluid. For the first time, such liquid is experimental studied by Choi, and Eastman [1]. Later, Buongiorno [2] has carried on an investigation regarding the heat transport phenomenon in nanofluids' flow. Non-linear convection flow of Williamson nanofluid through a radially stretching surface presented by Ibrahim et al. [3]. Khan et al. [4] examined the impacts of multi slip-on Jeffery fluid flow focus to a permeable stretched sheet. To transfer the nature of hybrid nanofluid convection inside a porous medium is scrutinized by [5]. Abbas et al. [6] investigated the different aspects of MHD cross nanofluid flow with the inspiration of thermal and joule heating. Zadeh et al. [7] numerically observe the flow, heat, and mass transfer of nano liquids over a vertical stretch sheet.

The stagnation point describes the liquid's movement near the stagnant region in front of the blunt flow body for the solid bodies floating in a fluid. In 1911 Hiemenz [8] introduced simulations of similarity to mathematical models, as well as the Navier–Stokes model introduced the concept of stagnant flow. Awaludin et al. [9] discover the stability analysis about the stagnation point flow over the shrinking/stretching sheet. The stagnation point flow about temperature and concentration over the stretching/shrinking sheet's dimensionless surface are investigated by Merkin and Pop [10]. Bhatti et al. [11] studied the effects of magnetizing on stagnation point flow over a shrinking sheet. To explore the impact of the variable thermal conductivity on the stagnation point flow reviewed by Shah et al. [12]. The effect of stagnation point flow on the micropolar based fluid over a permeable stretching plate examined by Fatunmbi and Adeniyan [13] along with the conclusion that an addition in the boundary parameter results in an increasing in the microrotation of the liquid constituents.

The current trend demonstrates that flow over wedge-shaped geometry has broad applications in the field of aerodynamics, heat exchangers, hydrodynamics, geothermal systems, groundwater pollution, oil recuperation, and so forth [14]. Falkner and Skan [15] acquired the flow over a static wedge brought about the advancement of the equation of Falkner–Skan. In the many previous years, numerous scientists have eventually contributed extraordinary eye-catching works on the Falkner–Skan flow in light of the impact of several thermophysical parameters [16]. Later, Watanabe [17] analyzed fluid flow behavior over a wedge with injection and suction, Ishak et al. [18] examined the MHD flow of past over the moving wedge. Ali et al. [19] obtained the numerical solution of the Falkner–Skan equation utilization the finite element numerical technique..

The investigation of chemical reaction finds enormous applications that incorporate food, contamination, the formation of fog, synthesis and oxidation materials, biochemical engineering, chemical processing types of equipment, plastic expulsion and metallurgy, and energy transfer in a drizzly cooling tower, and so on. The impact of the chemical reaction and the heat source/sink on the unsteady magnetohydrodynamic (MHD) flow of nanofluid over two equal radiating plates lowered in porous media briefly presented by Mohamed et al. [20]. The chemically reactive flow of magnetized Carreau nanofluid flow is a study by Ali et al. [21]. Muhammad et al. [22] studied the significance of nonlinear thermal radiation with a chemical reaction and Arrhenius activation energy in the 3D Eyring Powell nanofluids flow. Kalaivanan et al. [23] discussed the chemical reaction rate effects on second-grade nanofluid along with activation energy. The computational examination of chemically reactive fluid flow over a wedge shape geometry are investigated by Shahzad et al. [24]

Examination of non-Newtonian fluids attracts numerous scientist because of their significance in daily life and in mechanical and synthetic procedures. Taswar et al. [25] examined the MHD flow of tangent hyperbolic nanofluid along with the variable thickness. They found that the heat transfer rate was an increasing function of Prandtl number Pr. Examination of electro-magnetohydrodynamic (EMHD) non-Newtonian tangent hyperbolic nanofluid passed over a Riga plate considered by [26]. The main finding was that the modified Hartmann number maximize the skin friction coefficient and velocity of the fluid. Several numerical and analytical examinations have been reported to predict the characteristics of non-Newtonian fluids like, micropolar fluid [27], Casson fluid flow [28], Jeffrey nanofluid [29], non-Newtonian fluid flow [30], tangent hyperbolic fluid [31], micropolar nanofluid [32], and Oldroyd-B nanofluid [33].

In the previously mentioned investigation, for the most part, the wedge is either static or, on the other hand, moving. Less consideration is paid towards the tangent hyperbolic nanofluid flow across faster/slower stretching wedge. In this examination, five perspectives have been a focus. Firstly, to address the mass and heat transfer of tangent hyperbolic nanofluid. Secondly, to analyze the impact of thermal radiation. Thirdly, to examine the stagnation point flow. Fourthly, to study the effect of activation energy. Fifthly, the finite element approach for this elaborated problem. It solves boundary value problem adequately, rapidly and precisely [34–36]. The results have been computing on a finer mesh selected on the convergence criterion, where the solution's accuracy is ascertaining in special cases. Some expected outcomes are displayed and discussed.

2. Physical Model and Mathematical Formulation

2.1. Tangent Hyperbolic Constitutive Model

For the non-Newtonian fluids, there are numerous models in the literature which describe the different properties of a rheological fluid. The tangent hyperbolic fluid is one of the four constant non-Newtonian fluid models, describing the shear thinning behavior. The apparent viscosity gradually varies between zero and infinite shear rate. The constitutive equation for the tangent hyperbolic fluid is given by

$$\tau = [\mu_\infty + (\mu_0 + \mu_\infty)\tanh(\Gamma\dot{\omega})^\epsilon]\dot{\omega},$$

where, ϵ, τ, Γ, μ_0, and μ_∞ are the power law index, extra stress tensor, time constant, zero shear rate viscosity, and infinite shear rate viscosity, respectively, and $\dot{\omega}$ is defined as:

$$\dot{\omega} = \sqrt{\frac{1}{2}}\sqrt{\sum_i\sum_j \dot{\omega}_{ij}\dot{\omega}_{ji}} = \sqrt{\frac{1}{2}}\sqrt{\prod},$$

where $\prod$ is the second invariant of the strain rate tensor and $\prod = \frac{1}{2}\mathrm{tr}((\mathrm{grad}\ \mathbf{V})+(\mathrm{grad}\ \mathbf{V})^T)^2$. Consider the assumption $u_\infty = 0$. The fact, we are focusing on the shear thinning behaviour therefore $\Gamma\dot{\omega} < 1$, the extra stress tensor (τ) is reduced to

$$\tau = \mu_0[(\Gamma\dot{\omega})^\epsilon]\dot{\omega} = \mu_0[(1 + \Gamma\dot{\omega} - 1)^\epsilon]\dot{\omega} = \mu_0[1 + \epsilon(\Gamma\dot{\omega} - 1)]\dot{\omega},$$

2.2. Statement of the Problem

We assume a Falkner–Skan flow of an incompressible unsteady tangent hyperbolic nanofluid over a faster/slower stretching wedge in light of an applied magnetic field along with activation energy and magnetic field. The Reynolds number is considered very small, and prompted magnetic field would ignore. In current study, it has been considered that fluid flow is caused by stretching wedge with the velocity $\tilde{U}_w(x,t) = \frac{bx^m}{(1-ct)}$. The free stream velocity for the current problem is $\tilde{U}_e(x,t) = \frac{ax^m}{(1-ct)}$, where m, a, b, c are positive constants with $0 \leq m \leq 1$, and $ct < 1$ (see [37]). The angle of the wedge is supposed to be $\Omega = \pi\beta$, where $\beta = \frac{2m}{1+m}$ symbolizes the wedge angle parameter. From the perspective of White [38], positive value of β $(\beta > 0)$ provides acceleration to the fluid flow and negative value of β $(\beta < 0)$ generates retardation. Additionally, $\beta = 0$ (i.e., $m = 0$) corresponds to boundary layer flow over a horizontal flat plate and $\beta = 1$ (i.e., $m = 1$) relate to boundary layer flow near the stagnation point of a vertical flat plate. Further, we assume that (concentrations, temperature) at the wedge surface $(\tilde{C}_w, \tilde{T}_w)$ are higher than the ambient (concentrations, temperature) i.e., $(\tilde{C}_\infty, \tilde{T}_\infty)$ that is , $\tilde{C}_w > \tilde{C}_\infty$, and $\tilde{T}_w > \tilde{T}_\infty$. The Cartesian coordinates (x,y) is utilized with x correspond coincides with the surface of the wedge and y perpendicular to it, and $y \geq 0$ is the fluid occupied region (see Figure 1). Furthermore, the sheet is considered to be the hot fluid along with the wall defined as $-\kappa_f(\frac{\partial\tilde{T}}{\partial y}) = h_f(\tilde{T}_f - \tilde{T})$ (see [39,40]). A time-dependent magnetic field $B(t) = \frac{B_0}{(1-ct)^{1/2}}$ applied normal to the surface of wedge, the small magnetic Reynolds number is assumed, and impact of the induced magnetic field is neglected. Considering the above suppositions, the governing equations for the current modeled problem are as per the following [41,42]:

$$\frac{\partial \tilde{u}}{\partial x} + \frac{\partial \tilde{v}}{\partial y} = 0, \tag{1}$$

$$\frac{\partial \tilde{u}}{\partial t} + \tilde{u}\frac{\partial \tilde{u}}{\partial x} + \tilde{v}\frac{\partial \tilde{u}}{\partial y} = \frac{\partial \tilde{u}_e}{\partial t} + \tilde{u}_e\frac{\partial \tilde{u}_e}{\partial x} + \nu(1-\epsilon)\frac{\partial^2 \tilde{u}}{\partial y^2} + \sqrt{2}\nu\Gamma\epsilon\frac{\partial \tilde{u}}{\partial y}\frac{\partial^2 \tilde{u}}{\partial y^2} - \frac{\sigma B^2(t)\tilde{u}}{\rho}(\tilde{u}-\tilde{u}_e), \tag{2}$$

$$\frac{\partial \tilde{T}}{\partial t} + \tilde{u}\frac{\partial \tilde{T}}{\partial x} + \tilde{v}\frac{\partial \tilde{T}}{\partial y} = \frac{k_f}{\rho C_p}\frac{\partial^2 \tilde{T}}{\partial y^2} + \tau\tilde{D}_B\frac{\partial \tilde{C}}{\partial y}\frac{\partial \tilde{T}}{\partial y} + \tau\frac{\tilde{D}_T}{\tilde{T}_\infty}\left(\frac{\partial \tilde{T}}{\partial y}\right)^2 + \frac{Q_0}{\rho C_p}(\tilde{T}-\tilde{T}_\infty) - \frac{1}{\rho C_p}\frac{\partial q}{\partial y}, \tag{3}$$

$$\frac{\partial \tilde{C}}{\partial t} + \tilde{u}\frac{\partial \tilde{C}}{\partial x} + v\frac{\partial \tilde{C}}{\partial y} = \tilde{D}_B\frac{\partial^2 \tilde{C}}{\partial y^2} + \frac{\tilde{D}_T}{\tilde{T}_\infty}\frac{\partial^2 \tilde{T}}{\partial y^2} - k_r^2(\tilde{C}-\tilde{C}_\infty)\left(\frac{\tilde{T}}{\tilde{T}_\infty}\right)^n \exp\left(\frac{-E_a}{k_B\tilde{T}}\right), \tag{4}$$

$$\left.\begin{aligned} \tilde{u} = \tilde{U}_w(x) = \lambda_s\tilde{U}_e, \tilde{v} = \tilde{v}_w, \kappa_f(\frac{\partial \tilde{T}}{\partial y}) = h_f(\tilde{T}_f - \tilde{T}), \tilde{C} - \tilde{C}_w(x) = 0, \quad as \quad y = 0,\\ \tilde{u} \to \tilde{U}_e, \quad \tilde{T} \to \tilde{T}_\infty, \quad \tilde{C} \to \tilde{C}_\infty, \quad as \quad y \to \infty. \end{aligned}\right\} \tag{5}$$

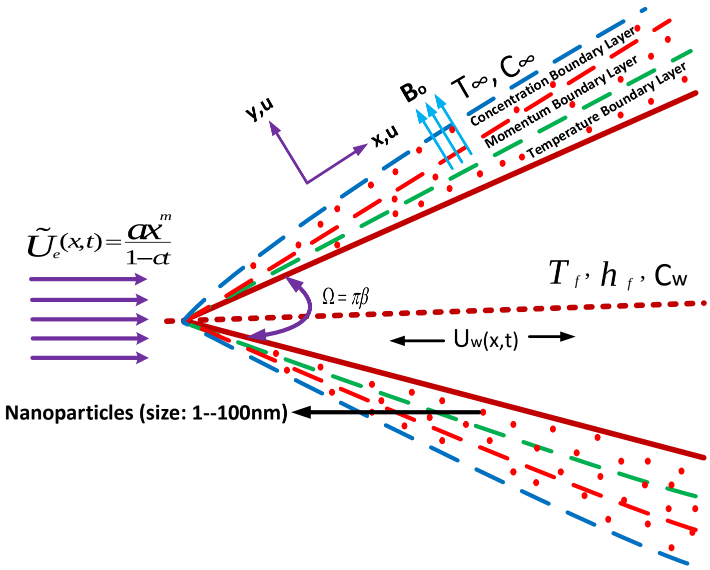

Figure 1. Physical and schematic configuration with coordinate system.

Here, $(\tilde{u}, \tilde{v})$ are velocity component in x, y directions, respectively, $\tilde{T}$ and $\tilde{C}$ are the fluid temperature and nanoparticle volume concentration, $\tilde{D}_B$ and $\tilde{D}_T$ are the Brownian diffusion and thermophoretic diffusion coefficient respectively, $\tilde{U}_e$ is the free stream velocity, B_0, m, ρ, C_p, E_a, ϵ, and Γ are the uniform magnetic field strength, Falkner–Skan power law parameter, fluid density, specific heat capacity, activation energy, the power law index, and Williamson parameter, respectively, Q_0 denotes the temperature-dependent volumetric rate of heat source ($Q_0 > 0$) and heat sink ($Q_0 < 0$), q_r is given by $q_r = \frac{4}{3}\frac{\alpha^*}{K_1}\frac{\partial \tilde{T}^4}{\partial y^2}$ (see[34,43]), here Stefan Boltzman constant is α^* and K_1 is the Roseland mean absorption coefficient, Further, the last term in Equation (4), $k_r^2(\tilde{C}-\tilde{C}_\infty)(\frac{\tilde{T}}{\tilde{T}_\infty})^n exp(\frac{-E_a}{k_B\tilde{T}})$ shows the modified Arrhenius equation with a reaction rate of k_r^2. Where $\tilde{T}_w$ and $\tilde{C}_w$ are temperature and nanoparticle volume fraction at the surface. The corresponding ambient values are denoted by $\tilde{T}_\infty$, $\tilde{C}_\infty$ respectively.

Introducing following similarity transformations(see [41,44]):

$$\psi(x,y,t)=\sqrt{\frac{2\nu x\tilde{U}_e}{(m+1)}}f(\zeta),\tilde{u}=\frac{\partial\psi}{\partial x}=\tilde{U}_e f'(\zeta),\tilde{v}=-\frac{\partial\psi}{\partial y}=-\sqrt{(\frac{m+1}{2})(\frac{\nu\tilde{U}_e}{x})}[f(\zeta)+(\frac{m-1}{m+1})\zeta f'(\zeta)],$$

$$\theta(\zeta)=\frac{\tilde{T}-\tilde{T}_\infty}{\tilde{T}_w-\tilde{T}_\infty},\ \phi(\zeta)=\frac{\tilde{C}-\tilde{C}_\infty}{\tilde{C}_w-\tilde{C}_\infty},\zeta=y\sqrt{\frac{(m+1)\tilde{U}_e}{2\nu x}}. \tag{6}$$

where ψ is the stream function and ζ is the dimensionless coordinate.

In view of Equation (6), Equations (2)–(5) transform into the following nonlinear ODE's:

$$[1-\epsilon+\epsilon Wef'']f'''+ff''-\beta(f'^2-1)-A(2-\beta)(\frac{\zeta}{2}f''+f'-1)-Ha^2(2-\beta)(f'-1)=0, \tag{7}$$

$$(1+Rd)\theta''+Pr(f\theta'-2f'\theta)+Pr[Nb\theta'\phi'+Nt(\theta')^2-\frac{A}{2}(2-\beta)(3\theta+\zeta\theta')+Q\theta]=0, \tag{8}$$

$$\phi''-\frac{A}{2}Le(2-\beta)(3\phi+\zeta\phi')+Le(f\phi'-2f'\phi)+\frac{Nt}{Nb}\theta''-2\Omega Le\phi(1+\gamma\theta)^n\exp(\frac{-EE}{1+\gamma\theta})=0, \tag{9}$$

$$\left.\begin{array}{l} f(\zeta)=f_w,\ f'(\zeta)=\lambda,\ \theta'(\zeta)=-Bi[1-\theta(\xi)],\ \phi(\zeta)=1\ at\ \zeta=0,\\ f'(\zeta)\to 1,\ \theta(\zeta)\to 0,\ \phi(\zeta)\to 0\ as\ \zeta\to\infty.\end{array}\right\} \tag{10}$$

The emerging parameters in Equations (07)-–(10) are defined as:

$$\lambda_s=\frac{\tilde{U}_w}{\tilde{U}e},\ A=\frac{c}{ax^{m-1}},\ Pr=\frac{\nu}{\tilde{\alpha}},\ Le=\frac{\nu}{\tilde{D}_B},\ R_d=\frac{16\sigma^*\tilde{T}_\infty^3}{3k^*K},\ Nb=\tau\tilde{D}_B(\nu)^{-1}(\tilde{C}_w-\tilde{C}_\infty),\ Nt=\frac{\tau\tilde{D}_T(\tilde{T}_w-\tilde{T}_\infty)}{\nu\tilde{T}_\infty},$$

$$EE=\frac{E_a}{\kappa_B\tilde{T}_\infty},\ Q=\frac{2Q_0x}{\tilde{U}_e(\rho C_p)}\ \Omega=\frac{xC_o(\kappa_r)^2}{\tilde{U}_w},\ \gamma=\frac{\tilde{T}_w-\tilde{T}_\infty}{\tilde{T}_\infty},\ \beta=\frac{2m}{m+1},\ Bi=-\frac{h_f}{\kappa_f}\left(\frac{(m+1)\tilde{U}_e}{2\nu x}\right)^{-\frac{1}{2}},$$

$$(Ha)^2=\frac{\sigma B_o^2}{\rho ax^{m-1}},\ We=\sqrt{\frac{\Gamma^2(m+1)(\tilde{U}_e)^3}{2\nu x}},\ Re_x=\frac{\tilde{U}_w(x)x}{\nu},\ f_w=-\frac{\tilde{v}_w}{\sqrt{\frac{(m+1)\nu\tilde{U}_e}{2x}}}.$$

where λ_s is the velocity ratio parameter of wedge such that $\lambda_s>1$ corresponds to faster stretching than that of free stream and $\lambda_s<1$ corresponds to slower than that of free stream flow [45], A is the unsteadiness parameter Pr is the Prandtl number, Le is the Lewis number, Rd is the radiation parameter, Nb, Nt are the Brownian motion and thermophoresis respectively, EE is the dimensionless activation energy, Q is the heat generation/absorption parameter, ω is the chemical reaction rate constant, γ is the temperature difference variable, β is the wedge angle parameter, Bi is the Biot number, Ha is the Hartmann number, We is the Weissenberg number, Re_x is the local Renolds number, and f_w is the suction/injection parameter ($f_w>0$ for suction and $f_w<0$ for injection). Skin friction coefficient expressions, local Nusselt number, and Sherwood number are defined as:

$$\tilde{C}_f=\frac{\tau_w}{\rho\tilde{U}^2{}_w},\ Nu=\frac{xq_w}{\kappa(\tilde{T}_w-\tilde{T}_\infty)},\ Shr=\frac{xq_m}{\tilde{D}_B(\tilde{C}_w-\tilde{C}_\infty)}. \tag{11}$$

where the skin friction tensor at wall is $\tau_w=\mu\left[(1-\epsilon)\frac{\partial\tilde{u}}{\partial y}+\frac{\epsilon\Gamma}{\sqrt{2}}\left(\frac{\partial\tilde{u}}{\partial y}\right)^2\right]_{y=0}$, the wall heat transfer is $q_w=-\kappa\left[(1+\frac{16\alpha\tilde{T}^3}{3\kappa})\frac{\partial\tilde{T}}{\partial y}\right]_{y=0}$, and the mass flux from the sheet is $q_m=-\left(\tilde{D}_B\frac{\partial\tilde{C}}{\partial y}\right)_{y=0}$. By the aid of similarity transformation Equation (7), we get:

$$\begin{cases} C_f Re_x^{1/2} = \sqrt{\frac{m+1}{2}}\Big[(1-\epsilon)f''(0) + \frac{\epsilon}{2}We\big(f''(0)\big)^2\Big], \\ Nu_x Re_x^{-\frac{1}{2}} = -\sqrt{\frac{m+1}{2}}\big[(Rd+1)\theta'(0)\big], \\ Shr_x Re_x^{\frac{-1}{2}} = -\sqrt{\frac{m+1}{2}}\big[\phi'(0)\big]. \end{cases} \tag{12}$$

3. Finite Element Solutions

The FEM (finite element method) is well known to solve various types of differential equations. This technique's basic idea is to comprise piecewise approximation of continuous polynomials functions that minimize the error size [46]. The fundamental steps and an outstanding description of this technique outlined by Jyothi [47], and Reddy [48]. It merits referencing that the finite element technique can solve the boundary value problem along with complex geometry precisely, rapidly, and accurately as compared to the finite difference method (FDM) [49,50] and solved many fluid-related engineering problems [51–54]. To solve the system of non-linear coupled partial differential Equations (7) to (9) together with boundary condition (10), firstly we consider:

$$f' = p, \tag{13}$$

The set of Equations (07)–(10) thus reduces to

$$[1-\epsilon+\epsilon Wep']p'' + fp' - \beta(p^2-1) - A(2-\beta)(\frac{\zeta}{2}p' + p - 1) - Ha^2(2-\beta)(p-1) = 0, \tag{14}$$

$$(1+Rd)\theta'' + Pr(f\theta' - 2p\theta) + Pr[Nb\theta'\phi' + Nt(\theta')^2 - \frac{A}{2}(2-\beta)(3\theta + \zeta\theta') + Q\theta] = 0, \tag{15}$$

$$\phi'' - \frac{A}{2}Le(2-\beta)(3\phi + \zeta\phi') + Le(f\phi' - 2p\phi) + \frac{Nt}{Nb}\theta'' - 2\Omega Le\phi(1+\gamma\theta)^n \exp(\frac{-EE}{1+\gamma\theta}) = 0, \tag{16}$$

$$\left.\begin{array}{l} f(\zeta) = f_w,\ p(\zeta) = \lambda,\ \theta'(\zeta) = -B_i[1-\theta(\zeta)],\ \phi(\zeta) = 1 \text{ at } \zeta = 0, \\ p(\zeta) \to 1,\ \theta(\zeta) \to 0,\ \phi(\zeta) \to 0 \text{ as } \zeta \to \infty. \end{array}\right\} \tag{17}$$

3.1. Variational-Formulations

The variational form connected with Equations (13)–(16) over a quadratic element $\Omega_\zeta = (\zeta_{\tilde{a}}, \zeta_{\tilde{a}+1})$ is given by

$$\int_{\zeta_{\tilde{a}}}^{\zeta_{\tilde{a}+1}} \tilde{w}_1\{\frac{df}{d\zeta} - p\}d\zeta = 0, \tag{18}$$

$$\begin{aligned} \int_{\zeta_{\tilde{a}}}^{\zeta_{\tilde{a}+1}} \tilde{w}_2\Big\{ & [1-\epsilon+\epsilon Wep']p'' + fp' - \beta(p^2-1) - A(2-\beta)(\frac{\zeta}{2}p' + p - 1) \\ & -Ha^2(2-\beta)(p-1)\Big\}d\zeta = 0, \end{aligned} \tag{19}$$

$$\int_{\zeta_{\tilde{a}}}^{\zeta_{\tilde{a}+1}} \tilde{w}_3\Big\{(1+Rd)\theta'' + Pr(f\theta' - 2p\theta) + Pr\Big[Nb\theta'\phi' + Nt(\theta')^2 - \frac{A}{2}(2-\beta)(3\theta+\zeta\theta') + Q\theta\Big]\Big\}d\zeta = 0, \tag{20}$$

$$\begin{aligned} \int_{\zeta_{\tilde{a}}}^{\zeta_{\tilde{a}+1}} \tilde{w}_4\Big\{ & \phi'' - \frac{A}{2}Le(2-\beta)(3\phi+\zeta\phi') + Le(f\phi' - 2p\phi) + \frac{Nt}{Nb}\theta'' \\ & -2\Omega Le\phi(1+\gamma\theta)^n \exp(\frac{-EE}{1+\gamma\theta})\Big\}d\zeta = 0. \end{aligned} \tag{21}$$

here $\tilde{w}_1, \tilde{w}_2, \tilde{w}_3$, and $\tilde{w}_4$ are trial functions.

3.2. Formulation of Finite-Element

The finite model of the element can be obtained from Equations (18)–(21) by replacing the following form:

$$\bar{f} = \sum_{n=1}^{3} \bar{f}_n \psi_n,\ \bar{p} = \sum_{n=1}^{3} \bar{p}_n \psi_n,\ \bar{\theta}' = \sum_{n=1}^{3} \bar{\theta}'_n \psi_n,\ \bar{\phi}' = \sum_{n=1}^{3} \bar{\phi}'_n \psi_n \tag{22}$$

with $\tilde{w}_1 = \tilde{w}_2 = \tilde{w}_3 = \tilde{w}_4 = \psi_n (n = 1, 2, 3)$, where the test functions ψ_n for a typical length element $\Omega_e = (\zeta_a, \zeta_{a+1})$ are given by.

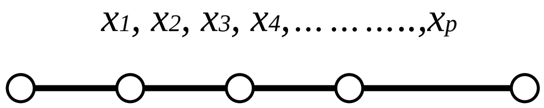

In global coordinates

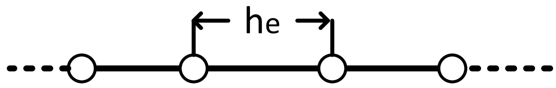

In local coordinates: For *p* = 2 (linear element)

$$\psi_1 = \frac{\zeta_{\tilde{a}+1} - \zeta}{\zeta_{\tilde{a}+1} - \zeta_{\tilde{a}}},\ \psi_2 = \frac{\zeta - \zeta_{\tilde{a}}}{\zeta_{\tilde{a}+1} - \zeta_{\tilde{a}}},\ \zeta_{\tilde{a}} \le \zeta \le \zeta_{\tilde{a}+1}. \tag{23}$$

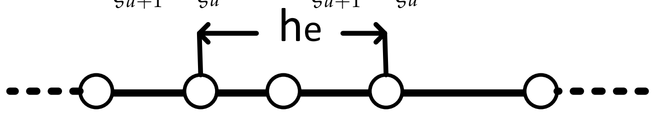

In local coordinates: For *p* = 3 (Quadratic element)

$$\psi_1 = \frac{(\zeta_{\tilde{a}+1} - \zeta_{\tilde{a}} - 2\zeta)(\zeta_{\tilde{a}+1} - \zeta)}{(\zeta_{\tilde{a}+1} - \zeta_{\tilde{a}})^2}, \quad \psi_2 = \frac{4(\zeta - \zeta_{\tilde{a}})(\zeta_{\tilde{a}+1} - \zeta)}{(\zeta_{\tilde{a}+1} - \zeta_{\tilde{a}})^2},$$
$$\psi_3 = -\frac{(\zeta_{\tilde{a}+1} - \zeta_{\tilde{a}} - 2\zeta)(\zeta - \zeta_{\tilde{a}})}{(\zeta_{\tilde{a}+1} - \zeta_{\tilde{a}})^2}, \quad \zeta_{\tilde{a}} \le \zeta \le \zeta_{\tilde{a}+1}. \tag{24}$$

The model of finite elements of the equations thus developed is given by:

$$\begin{bmatrix} [W^{11}] & [W^{12}] & [W^{13}] & [W^{14}] \\ [W^{21}] & [W^{22}] & [W^{23}] & [W^{24}] \\ [W^{31}] & [W^{32}] & [W^{33}] & [W^{34}] \\ [W^{41}] & [W^{42}] & [W^{43}] & [W^{44}] \end{bmatrix} \begin{bmatrix} \{f\} \\ \{p\} \\ \{\theta\} \\ \{\phi\} \end{bmatrix} = \begin{bmatrix} \{b^1\} \\ \{b^2\} \\ \{b^3\} \\ \{b^4\} \end{bmatrix} \tag{25}$$

where $[W^{mn}]$ and $[b^m]$ (m,n=1,2,3,4) are defined as:

$$\begin{aligned} W_{ij}^{11} &= \int_{\zeta_{\tilde{a}}}^{\zeta_{\tilde{a}+1}} \psi_i \frac{d\psi_j}{d\zeta} d\zeta, W_{ij}^{12} = -\int_{\zeta_{\tilde{a}}}^{\zeta_{\tilde{a}+1}} \psi_i \psi_j d\zeta,\ W_{ij}^{13} = W_{ij}^{14} = W_{ij}^{21} = 0, \\ W_{ij}^{22} &= -(1-\epsilon) \int_{\zeta_{\tilde{a}}}^{\zeta_{\tilde{a}+1}} \frac{d\psi_i}{d\zeta} \frac{d\psi_j}{d\zeta} d\zeta + We \int_{\zeta_{\tilde{a}}}^{\zeta_{\tilde{a}+1}} \bar{p''} \psi_i \frac{d\psi_j}{d\zeta} d\zeta + \int_{\zeta_{\tilde{a}}}^{\zeta_{\tilde{a}+1}} \bar{f} \psi_i \frac{d\psi_j}{d\zeta} d\zeta - Ha^2 (2-\beta) \int_{\zeta_{\tilde{a}}}^{\zeta_{\tilde{a}+1}} \psi_i \psi_j d\zeta \\ &- \beta \int_{\zeta_{\tilde{a}}}^{\zeta_{\tilde{a}+1}} \bar{p} \psi_i \psi_j d\xi - A(2-\beta) \int_{\zeta_{\tilde{a}}}^{\zeta_{\tilde{a}+1}} \psi_i \psi_j d\zeta - A(2-\beta) \frac{\zeta}{2} \int_{\zeta_{\tilde{a}}}^{\zeta_{\tilde{a}+1}} \psi_i \frac{d\psi_j}{d\zeta} d\zeta, W_{ij}^{23} = W_{ij}^{24} = W_{ij}^{31} = W_{ij}^{32} = 0, \end{aligned}$$

$$
\begin{aligned}
W_{ij}^{33} &= -(1+Rd)\int_{\zeta_a}^{\zeta_{a+1}} \frac{d\psi_i}{d\zeta}\frac{d\psi_j}{d\zeta}d\zeta + Pr\int_{\zeta_a}^{\zeta_{a+1}} \bar{f}\psi_i\frac{d\psi_j}{d\zeta}d\zeta - 2Pr\int_{\zeta_{\bar{a}}}^{\zeta_{\bar{a}+1}} \bar{p}\psi_i\psi_j d\zeta + PrNb\int_{\zeta_a}^{\zeta_{a+1}} \bar{\phi}'\psi_i\frac{d\psi_j}{d\zeta}d\zeta \\
&+ PrNt\int_{\zeta_a}^{\zeta_{a+1}} \bar{\theta}'\psi_i\frac{d\psi_j}{d\zeta}d\zeta - \frac{3PrA}{2}(2-\beta)\int_{\zeta_{\bar{a}}}^{\zeta_{\bar{a}+1}} \psi_i\psi_j d\zeta - APr(2-\beta)\frac{\zeta}{2}\int_{\zeta_{\bar{a}}}^{\zeta_{\bar{a}+1}} \psi_i\frac{d\psi_j}{d\zeta}d\zeta + PrQ\int_{\zeta_{\bar{a}}}^{\zeta_{\bar{a}+1}} \psi_i\psi_j d\zeta, \\
W_{ij}^{34} &= W_{ij}^{41} = W_{ij}^{42} = 0, W_{ij}^{43} = -\frac{Nt}{Nb}\int_{\zeta_a}^{\zeta_{a+1}} \frac{d\psi_i}{d\zeta}\frac{d\psi_j}{d\zeta}d\zeta, W_{ij}^{44} = -\int_{\zeta_a}^{\zeta_{a+1}} \frac{d\psi_i}{d\zeta}\frac{d\psi_j}{d\zeta}d\zeta + Le\int_{\zeta_a}^{\zeta_{a+1}} \bar{f}\psi_i\frac{d\psi_j}{d\zeta}d\zeta, \\
&- 2Le\int_{\zeta_{\bar{a}}}^{\zeta_{\bar{a}+1}} \bar{p}\psi_i\psi_j d\zeta - \frac{3LeA}{2}(2-\beta)\int_{\zeta_{\bar{a}}}^{\zeta_{\bar{a}+1}} \psi_i\psi_j d\zeta - ALe(2-\beta)\frac{\zeta}{2}\int_{\zeta_{\bar{a}}}^{\zeta_{\bar{a}+1}} \psi_i\frac{d\psi_j}{d\zeta}d\zeta \\
&- 2\Omega Le\int_{\zeta_{\bar{a}}}^{\zeta_{\bar{a}+1}} (1+\gamma\bar{\theta})^n \exp(\frac{-EE}{1+\gamma\bar{\theta}})\psi_i\psi_j d\zeta,
\end{aligned}
$$

and

$$
\begin{aligned}
&b_i^1 = 0,\ b_i^2 = -(1-\epsilon)\left(\psi\frac{dh}{d\zeta}\right)_{\zeta_{\bar{a}}}^{\zeta_{\bar{a}+1}} - \beta - A(2-\beta) - Ha^2(2-\beta), \\
&b_i^3 = -(1+Rd)\left(\psi\frac{d\theta_1}{d\zeta}\right)_{\zeta_{\bar{a}}}^{\zeta_{\bar{a}+1}}, b_i^4 = -\left(\psi\frac{d\phi}{d\zeta}\right)_{\zeta_{\bar{a}}}^{\zeta_{\bar{a}+1}} - \frac{Nt}{Nb}\left(\psi\frac{d\theta}{d\zeta}\right)_{\zeta_{\bar{a}}}^{\zeta_{\bar{a}+1}}
\end{aligned} \tag{26}
$$

with

$$
\bar{f} = \sum_{j=1}^{3}\bar{f}_j\psi_j,\ \bar{h} = \sum_{j=1}^{3}\bar{h}_j\psi_j,\ \bar{\theta}' = \sum_{j=1}^{3}\bar{\theta}_j'\psi_j,\ \bar{\phi}' = \sum_{j=1}^{3}\bar{\phi}_j'\psi_j.
$$

For computational purposes, the computational domain is divided into quadratic elements of equal size because Table 1 demonstrates no more variation against higher input of n (number of elements). Five functions are evaluated at each node, and 3005 × 3005 order of stiffness matrix is acquired after the assembling of whole element equations. After applying the boundary condition (Equation (20)), the developed equations are non-linear, so an iterative scheme utilized to solve it with 0.000005 required precision.

Table 1. Finite element method (FEM) convergence results of $f(\zeta)$, $p(\zeta)$, $\theta(\zeta)$, and $\phi(\zeta)$ at the 1.5 of computational domain [0, 12] for different number of elements when $Pr = 1$, $\lambda_s = 0.5$, $A = Q = We = 0.2$, $Ha = 0.5$, $Bi = EE = \gamma = 1$, $Nt = Nb = 0.3$, $\omega = 3$, $\epsilon = 0.3$, $Le = 3$, $Rd = 0.5$, $\beta = 0.5$, $n = 1$, $f_w = 0.5$.

Number of Elements	$f(1.5)$	$h(1.5)$	$\theta(1.5)$	$\phi(1.5)$
60	1.068133	0.914246	0.148457	0.054075
100	1.067776	0.914217	0.148492	0.054118
180	1.067636	0.914206	0.148507	0.054136
360	1.067585	0.914202	0.148512	0.054142
500	1.067582	0.914202	0.148513	0.054143
700	1.067578	0.914201	0.148513	0.054144
1000	1.067575	0.914201	0.148513	0.054144

4. Results And Discussion

Exploration for momentum, temperature and concentration fields are presented in pictorial form with consideration of three conditions at the boundary of geometric configuration viz wedge surface is stretched fast $(\lambda_s > 1)$, stretched uniformly $(\lambda_s = 1)$ and stretched slowly $(\lambda_s < 1)$. Tables 2 and 3 show a comparison of $f''(0)$ (skin contact coefficient) for certain values of the Hartmann number (Ha) and f_w (suction/injection). We observed from the tables, an excellent agreement is noticed which valid the acquired results. Further, to check the accuracy of finite element (FE) technique, a comparison of Nusselt number ($-Re_x^{1/2}Nu$) is performed with existing literature for higher input of Prandtl number Pr and wedge angle (β) in restricting cases. Here, an excellent agreement is also noticed (see Table 4). For numerical solutions, we have picked the non-dimensional parameter values $Pr = Bi = 1$, $\beta = Ha = Rd = 0.5$, $A = We = 0.2$, $Le = 3$, $Nb = Nt = 0.3$, $EE = n = 1$, $\Omega = 3$, $f_w = 0.5$, $\epsilon = 0.3$, $Q = 0.2$, $\gamma = 1$ these parameters values are saved as common in whole investigation of present study apart from the variations in the corresponding figures. In this investigation, the graphs in blue dashed line show the slower stretching sheet ($\lambda_s = 0.5$), the solid green colour indicate the stretched uniformly ($\lambda_s = 1$), and the solid red line represent the faster stretching sheet ($\lambda_s = 1.7$).

Table 2. Comparison of $f''(0)$ obtained by FEM and that of Ariel [55] for $\beta = 1$ and when all other parameters are fixed zero.

Ha	Ariel [55]			Current Results	% Error
	Perturbation Solution	**Approximate Solution**	**(a) Exact Solution**	**(b)**	$\lvert(\frac{b-a}{a})\rvert \times 100$
0.0	1.232588	1.224745	1.232588	1.232589	0.000081
0.4	1.295290	1.288410	1.295368	1.295369	0.000077
0.8	1.463725	1.462874	1.467976	1.467977	0.000068
1.0	1.570687	1.581139	1.585331	1.585332	0.000063
1.4	1.774774	1.840810	1.862848	1.862849	0.000161
1.6	1.842391	2.005172	2.017154	2.017155	0.000050
3.0	-	3.240355	3.240950	3.240952	0.000062
5.0	-	5.147815	5.147965	5.147968	0.000058
10.0	-	10.074740	10.074741	10.074748	0.000069

Table 3. Comparison of $f''(O)$ with f_w when $\beta = 1$ and all other parameters are fixed zero.

f_w	Ishak [56]	Ahmadand Khan [57]	Yin [58]	Imran Ullaha [59]	Postelnicu and Pop [60]	FEM Current Results
-1.0	0.7566	0.75655	0.75658	0.7566	0.75657	0.756576
-0.5	0.9692	0.96922	0.96923	0.9692	0.96923	0.969232
0.0	1.2326	1.23258	1.23259	1.2326	1.23259	1.232591
0.5	1.5418	1.54175	1.54175	1.5418	1.54175	1.541756
1.0	1.8893	1.88931	1.88931	1.8893	1.88931	1.889321

Table 4. Numerical values of Nusselt number $-Re^{1/2}Nu$ for different values of Prantdl number Pr and wedge angle parameter β when ϵ, We, Nt, Nb, f_w, Sc, and Ha are fixed zero.

Pr	White [38]		FEM (Current Results)	
	$\beta = 0$	$\beta = 0.3$	$\beta = 0$	$\beta = 0.3$
0.1	0.1980	0.2090	0.198129	0.209153
0.3	0.3037	0.3278	0.303719	0.327831
0.6	0.3916	0.4289	0.391677	0.428928
0.7	0.4178	0.4592	0.418094	0.459555
1.0	0.4696	0.5195	0.469604	0.519524
2.0	0.5972	0.6690	0.597241	0.669056
6.0	0.8672	0.9872	0.867297	0.987299
10.0	1.0297	1.1791	1.029779	1.179182

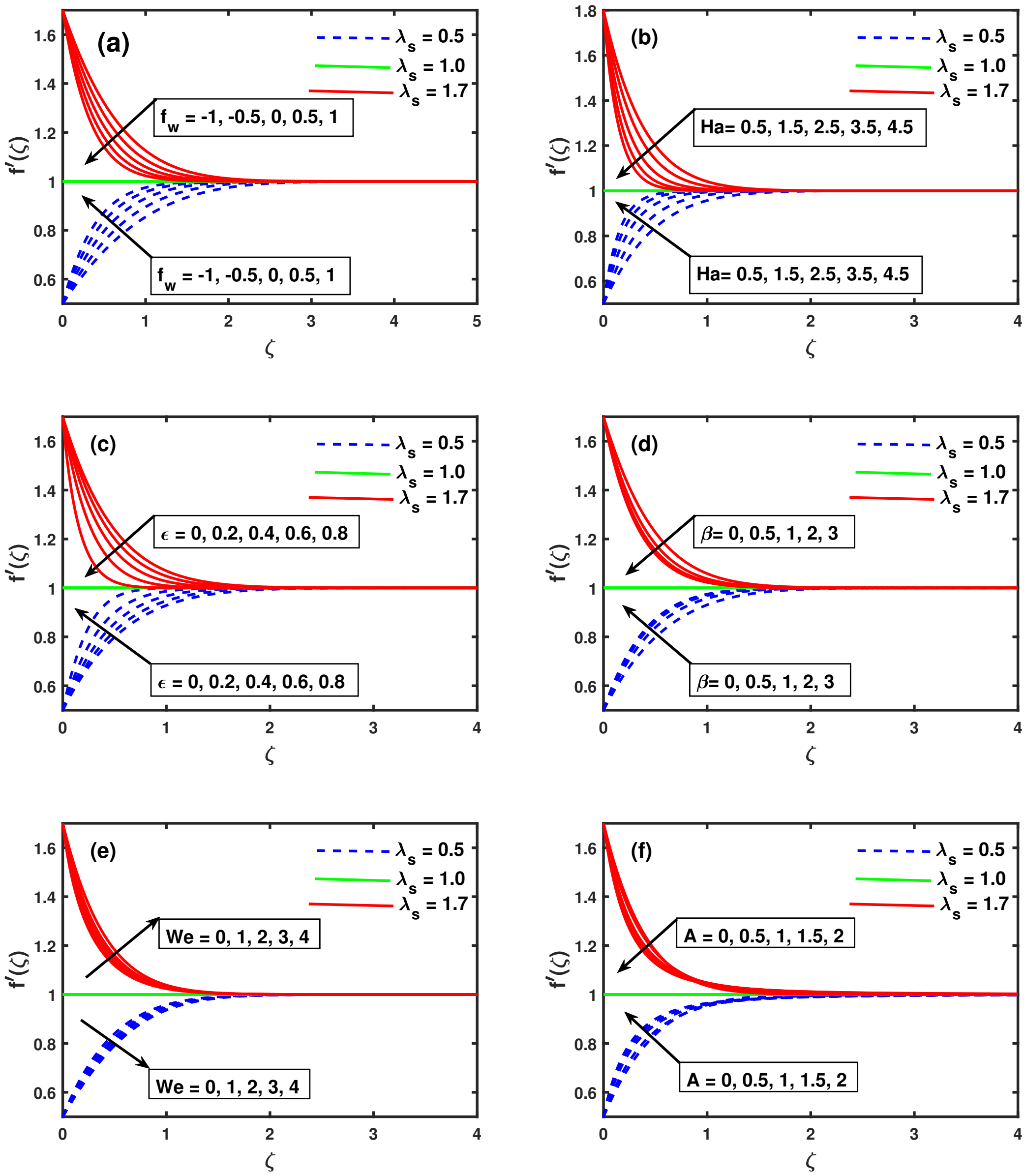

Figure 2. Fluctuation of $f'(\zeta)$ (velocity profile) along with f_w (suction/injection) (**a**), Hartmann number (Ha) (**b**), ϵ (material power law index) (**c**), β (wedge angle) (**d**), Weissenberg number (We) (**e**), and unsteadiness parameter (A) (**f**).

Plots in Figure 2a–f in their respective order represent the varying pattern of rescaled fluid velocity $f'(\zeta)$ concerning the appropriate changing values of the parameters f_w, Ha, ϵ, β, We and A. The velocity trace in the form of the parabola for $\lambda_s > 1$, it is a straight line for $\lambda_s = 1$, and it sweeps out an inverted boundary when $\lambda_s < 1$. Figure 2a illustrates that high values of injection parameter $(f_w < 0)$ makes the flow speedy in the boundary layer, whereas the suction $(f_w > 0)$ causes to slow the speed of flow. This outcome is in agreement with the influence of mass transfer at the boundary. The Hartman number's exceeding strength (Ha) decelerates the flow as depicted in Figure 2b. The very reason for this finding is the resistive force that calls into play due to the interaction of magnetic and electric fields. Figure 2c,d respectively exhibit the slowing speed of flow when material law index ϵ and wedge angle parameter (β) is an increment in case of $\lambda_s > 1$. An opposite phenomenon observes in the case of $\lambda_s < 1$. It is perceived that both these parameters impede the fluid flow. The rise in ϵ signifies the fluid's shear-thickening more extensive and an increase in α establishes the resistive force, which calls in to play due to the interaction of magnetic and electric fields. Weisenberg number (We), which corresponds to the increased relaxation time, Figure 2e discloses that with large values of We, the velocity recedes for $(\lambda_s < 1)$, but it becomes fast for $(\lambda_s > 1)$. Interestingly, the higher value of parameter A (unsteadiness) characterizes the more lapse of time after the jerk to the stretching surface. Hence, the slowing of velocity $(f'(\zeta))$ results, as revealed in Figure 2f.

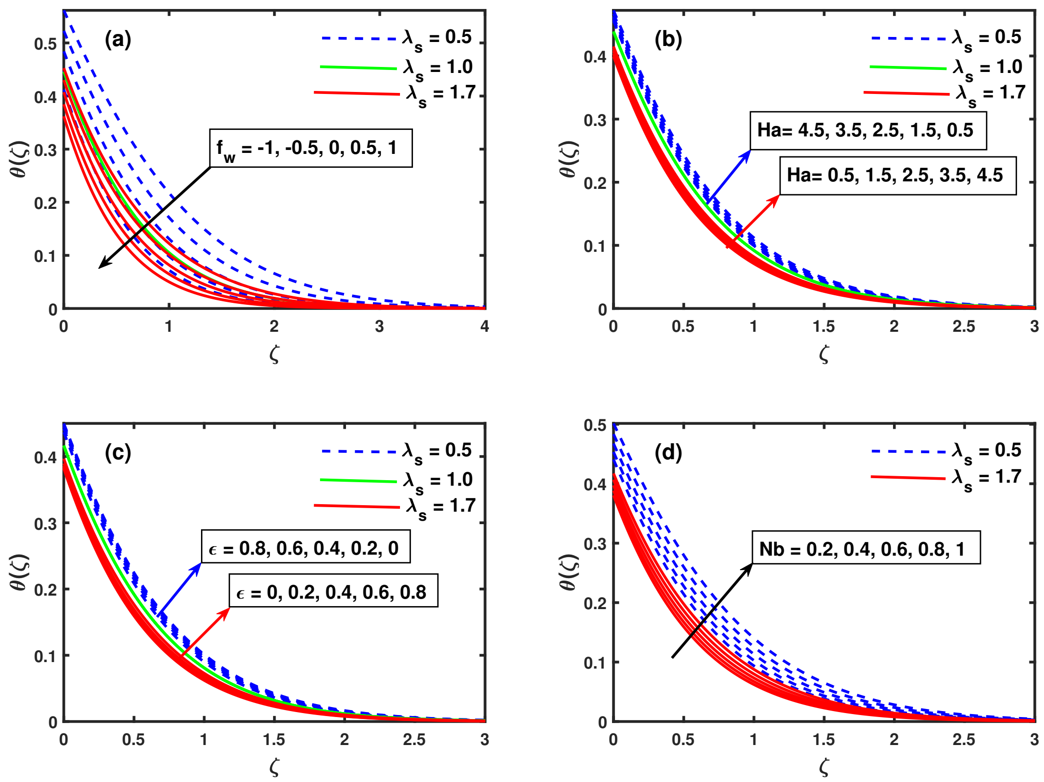

Figure 3. Fluctuation of temperature profile $(\theta(\zeta))$ along with f_w (suction/injection) (**a**), Hartmann number (Ha) (**b**), material power law index (ϵ) (**c**), and Brownian motion (Nb) (**d**).

A description for altering behavior of non-dimensional temperature $\theta(\zeta)$ is provided for $\lambda_s < 1$ (slow stretching) and $\lambda_s > 1$ (fast stretching). It observed that the temperature function for $(\lambda_s < 1)$ is larger than the case of $(\lambda_s > 1)$, as drawn in the following plots in Figure 3a–d to visualize respectively, the impacts of f_w, Ha, ϵ, and Brownian motion parameter Nb. A first sight reveals that larger injection$(f_w < 0)$ raises the curve of $\theta(\zeta)$ but higher suction $(f_w > 0)$ declines $\theta(\zeta)$. The magnetic field's intensified strength to yield greater value for Ha has enlarged $\theta(\zeta)$, and the thermal boundary layer loses its thickness (see Figure 3b). The physical reason for this outcome is associated with the enhanced resistance to the flow of fluid. Figure 3c,d respectively exhibit the effect of incremented values of ϵ and Nb resulted in higher temperature distribution because of the increasing ϵ, the shear thickening of fluid is enhanced to capture more heat, and the high value of Nb associated with the intensified random motion of the nanoparticles can efficiently diffuse heat in the fluid. Nt measures thermophoresis, and it stands for transportation of nanoparticles from hot to cold regions.

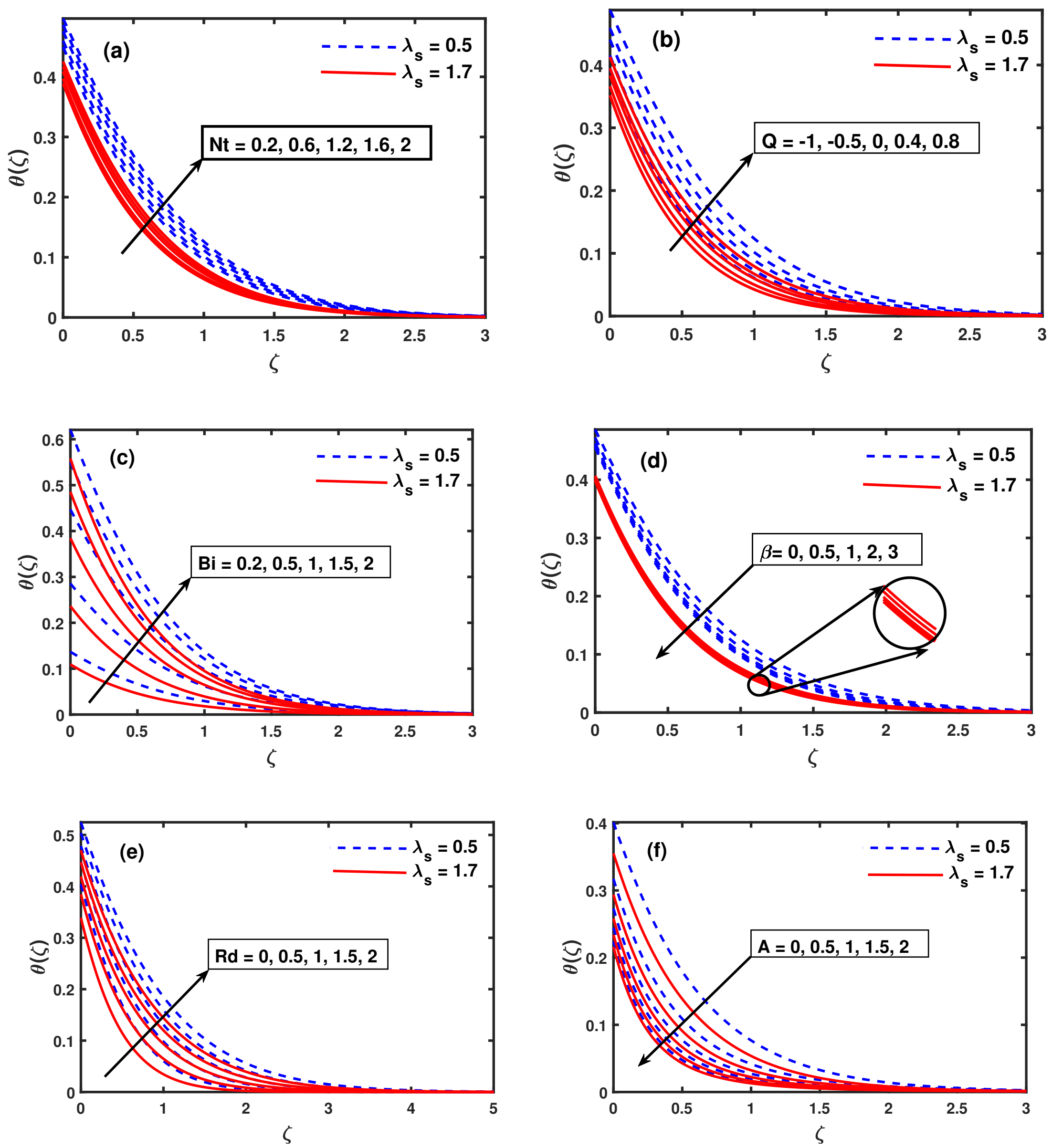

Figure 4. Fluctuation of temperature profile ($\theta(\zeta)$) along with thermophoresis (Nt) (**a**), heat generation/absorption (Q) (**b**), Biot number (Bi) (**c**), wedge angle (β) (**d**), radiation (Rd) (**e**), and unsteadiness parameter (A) (**f**).

Figure 4a discloses the directly proportional behavior of $\theta(\zeta)$ in response to Nt. Figure 4b placed to delineate $\theta(\zeta)$ with variation in Q, the heat sink-source parameter. As expected, it is revealed that $\theta(\zeta)$ diminishes against Q $(Q < 0)$ but it rises with Q $(Q > 0)$. Biot number is a measure of ratio for convection at the surface to conduction; hence $\theta(\zeta)$ is incremented when Bi made large as depicted in Figure 4c. The plot in Figure 4d presents the exposition that the incremented wedge parameter β has reduced temperature $\theta(\zeta)$. The radiation parameter Rd characterizes radiative heat transfer mode with a heat flux of greater strength at the surface. The temperature $\theta(\zeta)$ is raised directly with exceeding the value of Rd as indicated from Figure 4e. The increasing parameter of unsteadiness (A) marked significant depreciation in the values of $\theta(\zeta)$ as disclosed in Figure 5a–d in respective order display the non-dimensional volume fraction of nanoparticles $\phi(\zeta)$ under the influences of activation energy parameter EE, chemical reaction parameter Ω, f_w and Lewis number Le. It is perceived from these graphs that $\phi(\zeta)$ upsurges with increment in EE (see Figure 5a), but it diminishes against Ω, f_w, and Le (see Figure 5c,d).

Plots for the skin friction coefficient drawn under the variation of Ha and f_w. Figure 6a reveals that skin friction is intensified for larger values of Ha when there is slow stretching $(\lambda_s < 1)$ but opposite pattern is observed for fast stretching $(\lambda_s > 1)$. Moreover, the greater injection$(f_w < 0)$ reduces the skin friction but larger suction $(f_w > 0)$ enhances it when $\lambda_s < 1$. Mass transfer's role at the surface (suction/injection) is reverse when $\lambda_s > 1$. It is also seen skin friction remains uniform at zero value for static wedge $(\lambda_s = 1)$. The declining variation of Nusselt number against progressive values of thermophoresis and Brownian motion parameters Nt, Nb is sketched in Figure 6b. This situation disclosed that the Nusselt number is stronger for slow stretching than the wedge surface's fast stretching. Figure 6c implies that the Nusselt number enhances with the rising value of Prandtl number Pr as well as that of radiation parameter Rd. Here the Nusselt number is higher for $\lambda_s > 1$ but lower for $\lambda_s < 1$. The delineation of Sherwood number against activation energy parameter EE and chemical reaction parameter Ω is exposed in Figure 6d. It is perceived that Sherwood's number is enhanced when Ω elevated, but it is reduced vividly against developing values of EE. Moreover, Sherwood number attains higher values for $\lambda_s > 1$ as compared to those for $\lambda_s < 1$.

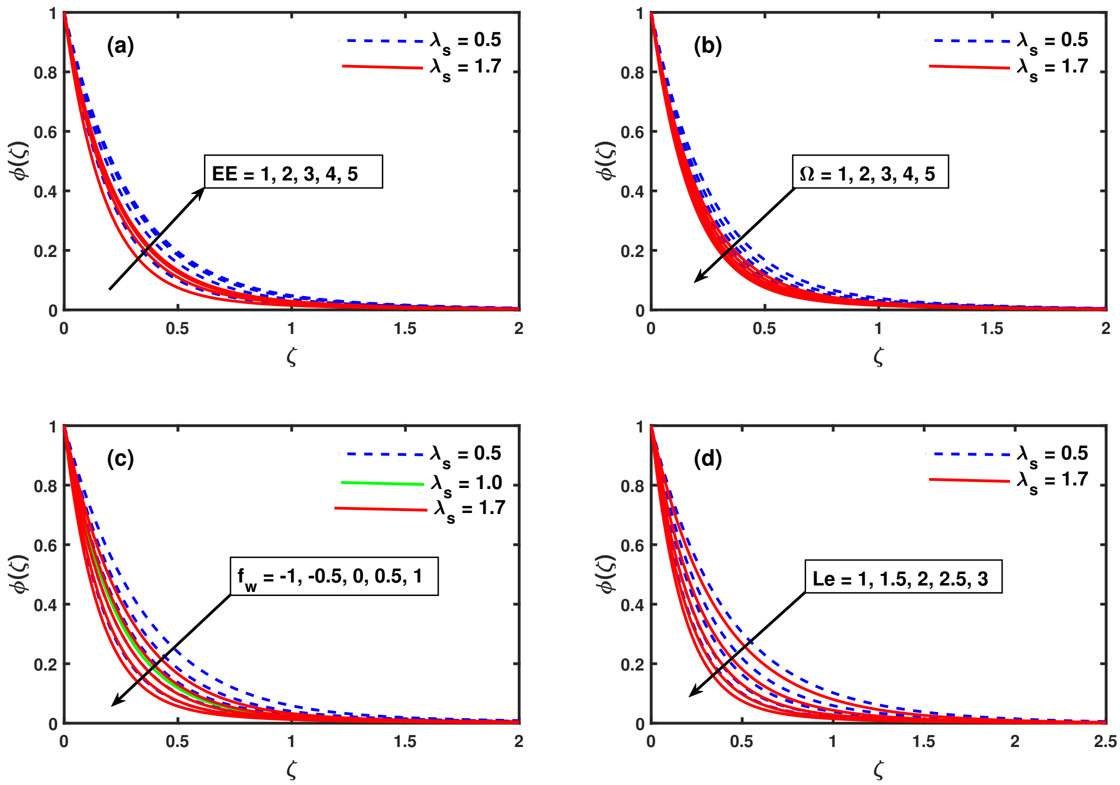

Figure 5. Fluctuation of nanoparticle concentration profile $(\phi(\zeta))$ along with activation energy (EE) (**a**), chemical reaction rate (Ω) (**b**), suction/injection (f_w) (**c**), and Lewis number (Le) (**d**).

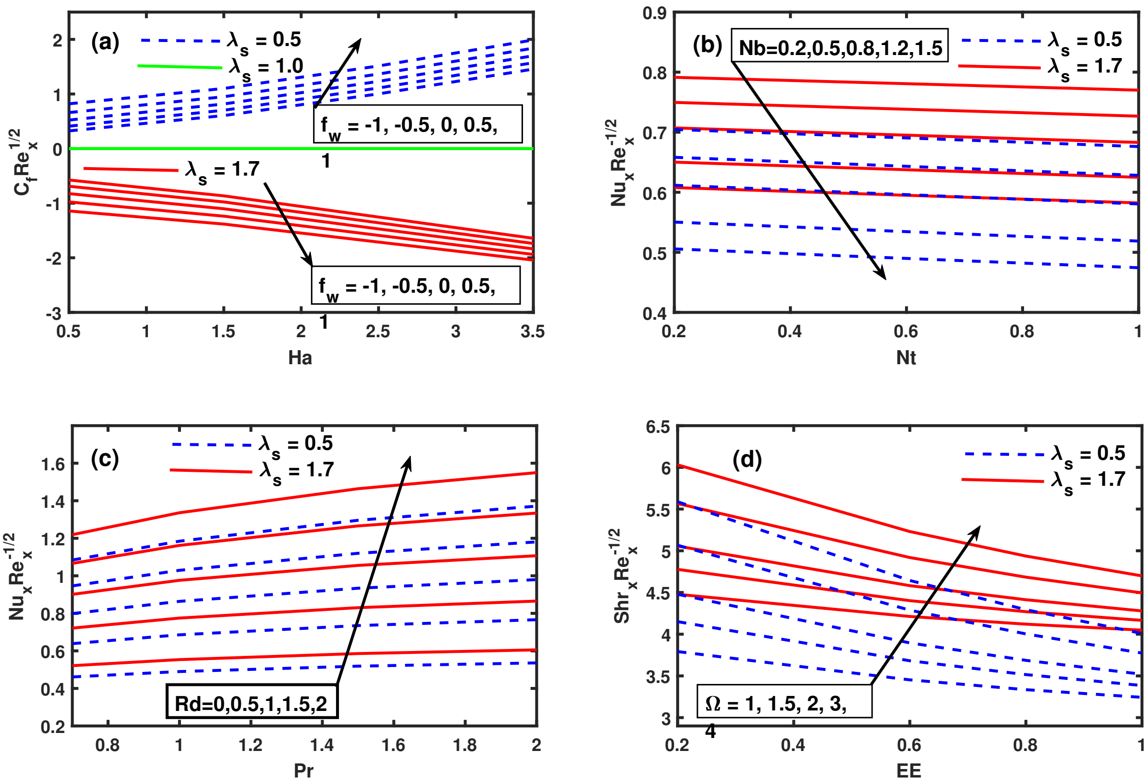

Figure 6. Fluctuation of $C_f Re_x^{1/2}$ (Skin friction coefficient) along with Hartmann number (Ha) and suction/injection (f_w) (**a**), Nusselt number ($Nu_x Re_x^{-1/2}$) with thermophoresis (Nt), Brownian motion (Nb) (**b**), Prandtl number (Pr), and radiation (Rd) (**c**), and Sherwood number ($Shr_x Re_x^{-1/2}$) along with activation energy (EE) and chemical reaction rate (Ω) (**d**).

5. Conclusions

The finite element solution for the unsteady motion of Carreau nanofluid over a fast or slow stretched wedge is explored in this work. The chemically reactive species of nanomaterial adheres to thermophoresis and Brownian movement slip conditions. Thermal transportation is base on a heat source, radiation mode, and convective boundary conditions. Some of the notable findings described briefly:

- Increased injection parameter $(f_w < 0)$ makes the flow faster, whereas the suction $(f_w > 0)$ causes the speed of flow to slow.
- The exceeding values of Hartman number Ha, suction/injection (f_w) material law index ϵ, aligned magnetic field parameter α and unsteadiness parameter (A) recede the velocity $f'(\zeta)$ when $\lambda_s > 1$ whereas enhance when $\lambda_s < 1$. An opposite trend is observed for Weissenberg number (We).
- The greater values of Nt, Rd, Bi, Q $(Q > 0)$ and Nb results in increased temperature distribution whereas the f_w, β, and unsteadiness (A) causes it to decline in both cases $(\lambda_s > 1, \lambda_s < 1)$.
- The greater values of Ha and ϵ results in increased temperature distribution when $\lambda_s > 1$ but a decline is observed for $\lambda_s < 1$.
- The volume fraction of nanoparticles $\phi(\zeta)$ is upsurged with increment in EE but it diminishes against Ω, f_w and Le in both cases $(\lambda_s > 1, \lambda_s < 1)$.
- Skin friction grows larger with increment in values of Ha when there is slow stretching $(\lambda_s < 1)$, but the opposite pattern is observed for fast stretching $(\lambda_s > 1)$.
- Nusselt number declines against progressive values of thermophoresis and Brownian motion parameters Nt, Nb.

Author Contributions: B.A. and R.A.N. modeled the problem and wrote the manuscript. A.M. complete the formal analysis and revision. O.M.A. thoroughly checked the mathematical modeling, English corrections, formal analysis, and revision. B.A. solved the problem using MATLAB software. L.A. and R.A.N.: writing—review and editing. All authors finalized the manuscript after its internal evaluation. All authors have read and agreed to the published version of the manuscript.

Funding: Researchers supporting project number (RSP-2020/61), King Saud University, Riyadh, Saudi Arabia.

Acknowledgments: This work is supported by the KIAS (Research Number: CG076601) and in part by Sejong University Faculty Research Fund.

Conflicts of Interest: The authors declare no conflicts of interest.

Nomenclature

$\tilde{T}$	Non-dimensional temperature
$\tilde{T}_w$	Temperature at surface
$\tilde{C}$	Non-dimensional nanoparticles concentration
$\tilde{C}_w$	Concentration at surface
$\tilde{T}_\infty$	Temperature away from the surface
a, b, c	Positive constants
$\tilde{C}_\infty$	Concentration away from the surface
E	Activation energy
$\tilde{n}_\infty$	Motile organisms away from the surface
$(\tilde{u}, \tilde{v})$	Velocity components
$\tilde{U}_w(x, t)$	Velocity of stretching/shrinking wedge
$\tilde{U}_e(x, t)$	Free stream velocity
β_T	Thermal expansion coefficient
ν	Kinematic viscosity
ρ_f	Density of fluid
Pr	Prandtl number
$\tilde{D}_T$	Thermophoretic diffusion coefficient
$\tilde{D}_B$	Brownian diffusion coefficient
m	Falkner-Skan power law
B_0	Uniform magnetic field
σ	Electrical conductivity
Le	Lewis number
β	Wedge angle parameter
We	Weissenberg number
ρCp	Base fluid heat capacity
Q_0	Heat generation/absorption
E	Activation energy
κ_B	Boltzmann constant
n	Fitted rate constant
σ^*	Stefan-Boltzmann number
K_1	Mean assimilation coefficient
ψ	Stream function
ϵ	Power law index
Γ	Williamson parameter
Nb	Brownian motion
Nt	Thermophoresis
ω	chemical reaction rate
Bi	Biot number
Ha	Hartmann number
Re_x	Local Renolds number

References

1. Choi, S.U.; Eastman, J.A. *Enhancing Thermal Conductivity of Fluids with Nanoparticles*; Argonne National Lab.: Lemont, IL, USA, 1995.
2. Buongiorno, J. Convective transport in nanofluids. *J. Heat Transf.* **2006**, *128*, 240–250. [CrossRef]
3. Ibrahim, W.; Gamachu, D. Nonlinear convection flow of Williamson nanofluid past a radially stretching surface. *AIP Adv.* **2019**, *9*, 085026. [CrossRef]
4. Khan, S.A.; Nie, Y.; Ali, B. Multiple slip effects on MHD unsteady viscoelastic nano-fluid flow over a permeable stretching sheet with radiation using the finite element method. *SN Appl. Sci.* **2020**, *2*, 66. [CrossRef]
5. Manh, T.D.; Nam, N.D.; Abdulrahman, G.K.; Moradi, R.; Babazadeh, H. Impact of MHD on hybrid nanomaterial free convective flow within a permeable region. *J. Therm. Anal. Calorim.* **2019**, *140*, 2865–2873 [CrossRef]
6. Abbas, S.; Khan, W.; Sun, H.; Ali, M.; Irfan, M.; Shahzed, M.; Sultan, F. Mathematical modeling and analysis of Cross nanofluid flow subjected to entropy generation. *Appl. Nanosci.* **2019**, *10*, 3149–3160. [CrossRef]
7. Zadeh, S.M.H.; Mehryan, S.; Sheremet, M.A.; Izadi, M.; Ghodrat, M. Numerical study of mixed bio-convection associated with a micropolar fluid. *Therm. Sci. Eng. Prog.* **2020**, *18*, 100539.
8. Hiemenz, K. Die Grenzschicht an einem in den gleichformigen Flussigkeitsstrom eingetauchten geraden Kreiszylinder. *Dinglers Polytech. J.* **1911**, *326*, 321–324.
9. Awaludin, I.; Weidman, P.; Ishak, A. Stability analysis of stagnation-point flow over a stretching/shrinking sheet. *AIP Adv.* **2016**, *6*, 045308. [CrossRef]
10. Merkin, J.H.; Pop, I. Stagnation point flow past a stretching/shrinking sheet driven by Arrhenius kinetics. *Appl. Math. Comput.* **2018**, *337*, 583–590. [CrossRef]
11. Bhatti, M.M.; Abbas, M.A.; Rashidi, M.M. A robust numerical method for solving stagnation point flow over a permeable shrinking sheet under the influence of MHD. *Appl. Math. Comput.* **2018**, *316*, 381–389. [CrossRef]
12. Shah, Z.; Kumam, P.; Deebani, W. Radiative MHD Casson Nanofluid Flow with Activation energy and chemical reaction over past nonlinearly stretching surface through Entropy generation. *Sci. Rep.* **2020**, *10*, 4402. [CrossRef] [PubMed]
13. Fatunmbi, E.; Adeniyan, A. MHD stagnation point-flow of micropolar fluids past a permeable stretching plate in porous media with thermal radiation, chemical reaction and viscous dissipation. *J. Adv. Math. Comput. Sci.* **2018**, 1–19. [CrossRef]
14. Leal, L.G. *Advanced Transport Phenomena: Fluid Mechanics and Convective Transport Processes*; Cambridge University Press: Cambridge, UK, 2007; Volume 7.
15. Falkneb, V.; Skan, S.W. LXXXV. Solutions of the boundary-layer equations. *Lond. Edinb. Dublin Philos. Mag. J. Sci.* **1931**, *12*, 865–896. [CrossRef]
16. Ali, B.; Hussain, S.; Nie, Y.; Rehman, A.U.; Khalid, M. Buoyancy Effetcs On FalknerSkan Flow of a Maxwell Nanofluid Fluid with Activation Energy past a wedge: Finite Element Approach. *Chin. J. Phys.* **2020**, *68*, 368–380. [CrossRef]
17. Watanabe, T. Thermal boundary layers over a wedge with uniform suction or injection in forced flow. *Acta Mech.* **1990**, *83*, 119–126. [CrossRef]
18. Ishak, A.; Nazar, R.; Pop, I. MHD boundary-layer flow past a moving wedge. *Magnetohydrodynamics* **2009**, *45*, 103–110.
19. Ali, B.; Hussain, S.; Nie, Y.; Khan, S.A.; Naqvi, S.I.R. Finite element simulation of bioconvection Falkner–Skan flow of a Maxwell nanofluid fluid along with activation energy over a wedge. *Phys. Scr.* **2020**, *95*, 095214. [CrossRef]
20. Mohamed, R.; Rida, S.; Arafa, A.; Mubarak, M. Heat and Mass Transfer in an Unsteady Magnetohydrodynamics Al_2O_3—Water Nanofluid Squeezed Between Two Parallel Radiating Plates Embedded in Porous Media With Chemical Reaction. *J. Heat Transf.* **2020**, *142*, 012401. [CrossRef]
21. Ali, B.; Rasool, G.; Hussain, S.; Baleanu, D.; Bano, S. Finite Element Study of Magnetohydrodynamics (MHD) and Activation Energy in Darcy–Forchheimer Rotating Flow of Casson Carreau Nanofluid. *Processes* **2020**, *8*, 1185. [CrossRef]
22. Muhammad, T.; Waqas, H.; Khan, S.A.; Ellahi, R.; Sait, S.M. Significance of nonlinear thermal radiation in 3D Eyring–Powell nanofluid flow with Arrhenius activation energy. *J. Therm. Anal. Calorim.* **2020**. [CrossRef]
23. Kalaivanan, R.; Ganesh, N.V.; Al-Mdallal, Q.M. An investigation on Arrhenius activation energy of second grade nanofluid flow with active and passive control of nanomaterials. *Case Stud. Therm. Eng.* **2020**, *22*, 100774. [CrossRef]
24. Shahzad, M.; Ali, M.; Sultan, F.; Khan, W.A.; Hussain, Z. Computational investigation of magneto-cross fluid flow with multiple slip along wedge and chemically reactive species. *Results Phys.* **2020**, *16*, 102972. [CrossRef]
25. Hayat, T.; Waqas, M.; Alsaedi, A.; Bashir, G.; Alzahrani, F. Magnetohydrodynamic (MHD) stretched flow of tangent hyperbolic nanoliquid with variable thickness. *J. Mol. Liq.* **2017**, *229*, 178–184. [CrossRef]
26. Mahdy, A.; Hoshoudy, G. EMHD time-dependant tangent hyperbolic nanofluid flow by a convective heated Riga plate with chemical reaction. *Proc. Inst. Mech. Eng. Part E J. Process. Mech. Eng.* **2019**, *233*, 776–786. [CrossRef]
27. Zaib, A.; Haq, R.U.; Sheikholeslami, M.; Chamkha, A.J.; Rashidi, M.M. Impact of non-darcy medium on mixed convective flow towards a plate containing micropolar water-based tio 2 nanomaterial with entropy generation. *J. Porous Media* **2020**, *23*, 11–26. [CrossRef]
28. Faraz, F.; Imran, S.M.; Ali, B.; Haider, S. Thermo-diffusion and multi-slip effect on an axisymmetric Casson flow over a unsteady radially stretching sheet in the presence of chemical reaction. *Processes* **2019**, *7*, 851. [CrossRef]
29. Abbas, M.A.; Bhatti, M.M.; Sheikholeslami, M. Peristaltic propulsion of Jeffrey nanofluid with thermal radiation and chemical reaction effects. *Inventions* **2019**, *4*, 68. [CrossRef]

30. Ali, L.; Xiaomin, L.; Ali, B.; Majeed, S.; Abdal, S. The Impact of Nanoparticles Due to Applied Magnetic Dipole in Micropolar Fluid Flow Using the Finite Element Method. *Symmetry.* **2020**, *12*, 520. [CrossRef]
31. Ramzan, M.; Gul, H.; Sheikholeslami, M. Effect of second order slip condition on the flow of tangent hyperbolic fluid—A novel perception of Cattaneo–Christov heat flux. *Phys. Scr.* **2019**, *94*, 115707. [CrossRef]
32. Ali, L.; Xiaomin, L.; Ali, B.; Majeed, S.; Abdal, S.; Ali, S.K. Analysis of Magnetic Properties of Nano-Particles Due to a Magnetic Dipole in Micropolar Fluid Flow over a Stretching Sheet. *Coatings* **2020**, *10*, 170. [CrossRef]
33. Ali, B.; Hussain, S.; Nie, Y.; Hussein, A.K.; Habib, D. Finite element investigation of Dufour and Soret impacts on MHD rotating flow of Oldroyd-B nanofluid over a stretching sheet with double diffusion Cattaneo Christov heat flux model. *Powder Technol.* **2021**, *377*, 439–452. [CrossRef]
34. Ali, L.; Liu, X.; Ali, B.; Mujeed, S.; Abdal, S. Finite Element Analysis of Thermo-Diffusion and Multi-Slip Effects on MHD Unsteady Flow of Casson Nano-Fluid over a Shrinking/Stretching Sheet with Radiation and Heat Source. *Appl. Sci.* **2019**, *9*, 5217. [CrossRef]
35. Ali, B.; Nie, Y.; Hussain, S.; Manan, A.; Sadiq, M.T. Unsteady magneto-hydrodynamic transport of rotating Maxwell nanofluid flow on a stretching sheet with Cattaneo–Christov double diffusion and activation energy. *Therm. Sci. Eng. Prog.* **2020**, *20*, 100720. [CrossRef]
36. Ali, B.; Naqvi, R.A.; Hussain, D.; Aldossary, O.M.; Hussain, S. Magnetic Rotating Flow of a Hybrid Nano-Materials Ag-MoS_2 and Go-MoS_2 in $C_2H_6O_2$-H_2O Hybrid Base Fluid over an Extending Surface Involving Activation Energy: FE Simulation. *Mathematics* **2020**, *8*, 1730. [CrossRef]
37. Shahzad, A.; Ali, R.; Hussain, M.; Kamran, M. Unsteady axisymmetric flow and heat transfer over time-dependent radially stretching sheet. *Alex. Eng. J.* **2017**, *56*, 35–41. [CrossRef]
38. White, F.M. *Viscous Fluid Flow*; Magraw-Hill Inc.: New York, NY, USA, 1991.
39. Ali, B.; Naqvi, R.A.; Nie, Y.; Khan, S.A.; Sadiq, M.T.; Rehman, A.U.; Abdal, S. Variable Viscosity Effects on Unsteady MHD an Axisymmetric Nanofluid Flow over a Stretching Surface with Thermo-Diffusion: FEM Approach. *Symmetry* **2020**, *12*, 234. [CrossRef]
40. Ali, B.; Yu, X.; Sadiq, M.T.; Rehman, A.U.; Ali, L. A Finite Element Simulation of the Active and Passive Controls of the MHD Effect on an Axisymmetric Nanofluid Flow with Thermo-Diffusion over a Radially Stretched Sheet. *Processes* **2020**, *8*, 207. [CrossRef]
41. Akbar, N.S.; Nadeem, S.; Haq, R.U.; Khan, Z. Numerical solutions of Magnetohydrodynamic boundary layer flow of tangent hyperbolic fluid towards a stretching sheet. *Indian J. Phys.* **2013**, *87*, 1121–1124. [CrossRef]
42. Ilias, M.R.; Rawi, N.A.; Zaki, N.H.M.; Shafie, S. Aligned MHD Magnetic Nanofluid Flow Past a Static Wedge. *Int. J. Eng. Technol.* **2018**, *7*, 28–31. [CrossRef]
43. Abdal, S.; Ali, B.; Younas, S.; Ali, L.; Mariam, A. Thermo-Diffusion and Multislip Effects on MHD Mixed Convection Unsteady Flow of Micropolar Nanofluid over a Shrinking/Stretching Sheet with Radiation in the Presence of Heat Source. *Symmetry* **2020**, *12*, 49. [CrossRef]
44. Raju, C.; Hoque, M.M.; Sivasankar, T. Radiative flow of Casson fluid over a moving wedge filled with gyrotactic microorganisms. *Adv. Powder Technol.* **2017**, *28*, 575–583. [CrossRef]
45. Ullah, I.; Shafie, S.; Khan, I. MHD heat transfer flow of Casson fluid past a stretching wedge subject to suction and injection. *Malays. J. Fundam. Appl. Sci.* **2017**, *13*, 637–641. [CrossRef]
46. Reddy, G.J.; Raju, R.S.; Rao, J.A. Influence of viscous dissipation on unsteady MHD natural convective flow of Casson fluid over an oscillating vertical plate via FEM. *Ain Shams Eng. J.* **2018**, *9*, 1907–1915. [CrossRef]
47. Jyothi, K.; Reddy, P.S.; Reddy, M.S. Carreau nanofluid heat and mass transfer flow through wedge with slip conditions and nonlinear thermal radiation. *J. Braz. Soc. Mech. Sci. Eng.* **2019**, *41*, 415. [CrossRef]
48. Reddy, J.N. *Solutions Manual for an Introduction to the Finite Element Method*; McGraw-Hill: New York, NY, USA, 1993; p. 41.
49. Ibrahim, W.; Gadisa, G. Finite element solution of nonlinear convective flow of Oldroyd-B fluid with Cattaneo-Christov heat flux model over nonlinear stretching sheet with heat generation or absorption. *Propuls. Power Res.* **2020**, *55*, 304–315. [CrossRef]
50. Ali, B.; Hussain, S.; Abdal, S.; Mehdi, M.M. Impact of Stefan blowing on thermal radiation and Cattaneo–Christov characteristics for nanofluid flow containing microorganisms with ablation/accretion of leading edge: FEM approach. *Eur. Phys. J. Plus* **2020**, *135*, 1–18. [CrossRef]
51. Ali, B.; Nie, Y.; Khan, S.A.; Sadiq, M.T.; Tariq, M. Finite Element Simulation of Multiple Slip Effects on MHD Unsteady Maxwell Nanofluid Flow over a Permeable Stretching Sheet with Radiation and Thermo-Diffusion in the Presence of Chemical Reaction. *Processes* **2019**, *7*, 628. [CrossRef]
52. Khan, S.A.; Nie, Y.; Ali, B. Multiple Slip Effects on Magnetohydrodynamic Axisymmetric Buoyant Nanofluid Flow above a Stretching Sheet with Radiation and Chemical Reaction. *Symmetry* **2019**, *11*, 1171. [CrossRef]
53. Uddin, M.; Rana, P.; Bég, O.A.; Ismail, A.M. Finite element simulation of magnetohydrodynamic convective nanofluid slip flow in porous media with nonlinear radiation. *Alex. Eng. J.* **2016**, *55*, 1305–1319. [CrossRef]
54. Ibrahim, W.; Gadisa, G. Finite Element Method Solution of Boundary Layer Flow of Powell-Eyring Nanofluid over a Nonlinear Stretching Surface. *J. Appl. Math.* **2019**, *2019*, 3472518. [CrossRef]
55. Ariel, P. Hiemenz flow in hydromagnetics. *Acta Mech.* **1994**, *103*, 31–43. [CrossRef]

56. Ishak, A.; Nazar, R.; Pop, I. Falkner-Skan equation for flow past a moving wedge with suction or injection. *J. Appl. Math. Comput.* **2007**, *25*, 67–83. [CrossRef]
57. Ahmad, R.; Khan, W.A. Effect of viscous dissipation and internal heat generation/absorption on heat transfer flow over a moving wedge with convective boundary condition. *Heat Transf. Res.* **2013**, *42*, 589–602. [CrossRef]
58. Yih, K. MHD forced convection flow adjacent to a non-isothermal wedge. *Int. Commun. Heat Mass Transf.* **1999**, *26*, 819–827. [CrossRef]
59. Ullah, I.; Shafie, S.; Khan, I. Heat generation and absorption in MHD flow of Casson fluid past a stretching wedge with viscous dissipation and newtonian heating. *J. Teknol.* **2018**, *1–9*. [CrossRef]
60. Postelnicu, A.; Pop, I. Falkner–Skan boundary layer flow of a power-law fluid past a stretching wedge. *Appl. Math. Comput.* **2011**, *217*, 4359–4368. [CrossRef]